

Pump-probe spectroscopy of the one-dimensional extended Hubbard model at half filling

Koudai Sugimoto^{1,*} and Satoshi Ejima²

¹*Department of Physics, Keio University, Yokohama 223-8522, Japan*

²*Institut für Softwaretechnologie, Abteilung High-Performance Computing, Deutsches Zentrum für Luft- und Raumfahrt (DLR), 22529 Hamburg, Germany*

(Dated: May 18, 2023)

By utilizing time-dependent tensor-network algorithms in the (infinite) matrix-product-state representation, we theoretically investigate the pump-probe spectroscopy of the one-dimensional extended Hubbard model at half filling. Our focus lies on nonequilibrium optical conductivity and time- and angle-resolved photoemission spectroscopy experiments. In the spin-density-wave (SDW) phase, we identify an in-gap state in the nonequilibrium optical conductivity due to the formation of excitons (or doublon-holon pairs), generated by the pulse through nonlocal interactions. In the strong-coupling regime, we discern additional multiple in-gap and out-of-gap states. In the charge-density-wave (CDW) phase, we detect not only an in-gap state but also a finite Drude weight, which results from the dissolution of charge order by photoexcitation. Analyzing time-dependent single-particle excitation spectra directly in the thermodynamic limit confirms the origin of these new states in the SDW and CDW phases as the excitation of newly emerged dispersions. Our study illustrates that the pump-probe spectroscopy simulations in the thermodynamic limit furnish unambiguous spectral structures that allow for direct comparison with experimental results, and the integration of nonequilibrium optical conductivity and time- and angle-resolved photoemission spectroscopy provides comprehensive insights into nonequilibrium states.

I. INTRODUCTION

Recent years have seen significant progress in studying novel phenomena in materials driven out of equilibrium by high-intensity laser irradiation [1, 2]. Emergent phenomena, such as photoinduced (photoenhanced) superconductivity [3–13] and optical control of magnetic order [14–21] in strongly correlated electron systems, have also started to attract both experimental and theoretical attention. In this context, pump-probe spectroscopy has been a crucial tool for exploring nonequilibrium phenomena in these materials. This technique involves exciting a system with a high-intensity pump pulse, followed by examining the dynamical properties of the nonequilibrium state through the linear response of a low-intensity probe pulse.

Analyzing the nonequilibrium state of strongly correlated systems within a one-dimensional (1D) model provides a beneficial starting point since the theoretical treatment of a 1D system is simpler compared to two- or three-dimensional systems. Despite being a special case, essential characteristics of correlated systems can be elucidated from 1D systems. Furthermore, the 1D Mott insulator, which manifests in actual materials and has been thoroughly studied in the literature, is of particular interest. Ultrafast phenomena of 1D Mott insulators, such as organic salt ET-F₂TCNQ [22–26] and halogen-bridged transition-metal compounds [27–29], have been intensively explored in preceding experiments because their optical response is significantly influenced by the

formation of doublon-holon bound states due to nonlocal interactions resulting from photoexcitation.

From a theoretical perspective, photoinduced nonequilibrium states in the model with nonlocal interaction have been discussed in the literature [11, 30–36]. Numerical simulations of pump-probe spectroscopy have reported the emergence of light-induced in-gap states in the half-filled 1D extended Hubbard model (1DEHM) including nearest-neighbor Coulomb interaction. This was achieved by examining the nonequilibrium optical conductivity using time-dependent exact diagonalization [37] and density-matrix renormalization group [38] techniques. However, previous studies have shown system-size dependencies in their results since their calculations were conducted using finite clusters.

In this study, by employing time-dependent tensor-network algorithms in the infinite matrix-product state (iMPS) representation, we simulate the nonequilibrium dynamics of the 1DEHM directly in the thermodynamic limit to investigate nonequilibrium phenomena induced by an intense, short-time pulse. We elucidate the dynamical properties of this system by examining the linear response of a subsequent weak probe pulse, corresponding to pump-probe spectroscopy experiments. Our focus lies primarily on optical conductivity and time- and angle-resolved photoemission spectroscopy (TARPES) in nonequilibrium situations.

Calculating with an infinite system offers the advantage of distinguishing excitation spectra originating from continuous levels from those from discrete levels. In finite-system analyses, spectra may appear discretized even if the excitation derives from continuous levels. By directly simulating an infinite system, this issue can be circumvented. Additionally, thanks to the high-

* sugimoto@rk.phys.keio.ac.jp

resolution calculation concerning momentum, we can easily obtain detailed peak structure and dispersion relations, facilitating unambiguous comparisons between theory and experiments. Furthermore, we demonstrate that the nonequilibrium dynamics can be comprehensively understood by studying both optical conductivity and TARPES in a complementary fashion. This study aims to deepen the understanding of nonequilibrium phenomena in strongly correlated electron systems and provide valuable insights for experimental investigations.

The remainder of this paper is organized as follows. In Sec. II, we introduce the 1DEHM and describe the numerical method used in this study. In Sec. III, we present the numerical results of nonequilibrium optical conductivity induced by an intense pump pulse. In Sec. IV, we demonstrate the simulated single-particle excitation spectra, which are expected to be observed in TARPES experiments. Finally, we provide conclusions and future outlook in Sec. V.

II. MODEL AND METHOD

In this section, we introduce the Hamiltonian of the 1DEHM and provide a brief explanation of the numerical calculations that we performed.

A. Extended Hubbard model

We consider the 1DEHM at half filling. Under the influence of a spatially uniform vector potential $A(t)$, the Hamiltonian is written as

$$\begin{aligned} \hat{H}(t) = & -t_h \sum_{j,\sigma} \left(e^{iA(t)} \hat{c}_{j,\sigma}^\dagger \hat{c}_{j+1,\sigma} + \text{H.c.} \right) \\ & + U \sum_j \left(\hat{n}_{j,\uparrow} - \frac{1}{2} \right) \left(\hat{n}_{j,\downarrow} - \frac{1}{2} \right) \\ & + V \sum_j (\hat{n}_j - 1)(\hat{n}_{j+1} - 1), \end{aligned} \quad (1)$$

where $\hat{c}_{j,\sigma}$ ($\hat{c}_{j,\sigma}^\dagger$) is the annihilation (creation) operator of an electron at site j with spin σ , t_h is the hopping integrals of electrons, U is the on-site interaction, and V is the intersite interaction. We define the number operators of the electrons as $\hat{n}_{j,\sigma} = \hat{c}_{j,\sigma}^\dagger \hat{c}_{j,\sigma}$ and $\hat{n}_j = \sum_\sigma \hat{n}_{j,\sigma}$. In the strong-coupling limit, where $U, V \gg t_h$, the ground state (GS) of this model exhibits a spin-density wave (SDW) state for $U \gtrsim 2V$ and a charge-density wave (CDW) state for $U \lesssim 2V$ [39]. Note that the SDW-CDW transition occurs at $V/t_h \approx 5.124$ for $U/t_h = 10$. Hereafter, we use $t_h = 1$.

B. Time evolution

We simulate the time-dependent quantum state under a high-intensity laser pulse with a vector potential given by

$$A(t) = A_0 e^{-(t-t_0)^2/2\sigma_0^2} \cos(\omega_0 t), \quad (2)$$

where A_0 is the amplitude, t_0 is the central time, σ_0 is the width, and ω_0 is the frequency of the pump light. To numerically calculate the GS and the time-evolution dynamics, we employ the infinite time-evolving block decimation (iTEBD) method [40, 41]. The quantum state at time t is denoted as $|\psi(t)\rangle$, and we set $|\psi(-\infty)\rangle$ as the GS obtained by carrying out the imaginary-time evolution. We represent the time-evolution operator from t' to t as $\hat{U}(t,t') = \mathcal{T} \exp\left(-i \int_{t'}^t dt'' \hat{H}(t'')\right)$, where \mathcal{T} is the time-ordering operator, allowing us to write $|\psi(t)\rangle = \hat{U}(t, -\infty) |\psi(-\infty)\rangle$. We denote the expectation value at time t as $\langle \cdots \rangle_t = \langle \psi(t) | \cdots | \psi(t) \rangle$.

In the following section, we investigate nonequilibrium dynamics when a pump pulse is applied to both the SDW and CDW states of the 1DEHM. Namely, we focus on nonequilibrium optical conductivity and single-particle excitation spectra. For pump-pulse parameters, we fix $\sigma_0 = 0.5$ and set $A_0 = 0.3$ for $V \neq 0$ and $A_0 = 0.6$ for $V = 0$. To efficiently generate nonequilibrium states, ω_0 is set to the value where the optical conductivity in the GS becomes the largest for each V . Optical conductivities in the GS for various V are given in the next section.

In the time-evolution calculations for optical conductivity and single-particle excitation spectra, we set the time step to $\delta t = 0.01$ and $\delta t = 0.05$, respectively, and the bond dimensions to $\chi = 3000$ and $\chi = 1500$, respectively. We apply the fourth-order Trotter decomposition for optical conductivity and the second-order one for single-particle excitation spectra.

III. NONEQUILIBRIUM OPTICAL CONDUCTIVITY

We estimate the optical conductivity by examining the response of an electric current to a weak electric field. The current operator in a vector potential $A(t)$ is written as

$$\hat{J}_{A(t)} = -\frac{\partial \hat{H}}{\partial A} = t_h \sum_{j,\sigma} \left(i e^{iA(t)} \hat{c}_{j,\sigma}^\dagger \hat{c}_{j+1,\sigma} + \text{H.c.} \right). \quad (3)$$

Upon applying a weak electric field $E_{\text{pr}}(t) = -\partial A_{\text{pr}}(t)/\partial t$ as a probe pulse in addition to the pump pulse, the induced deviation in the current per site satisfies

$$j_{\text{pr}}(t) = \frac{1}{L} \left(\langle \hat{J}_{A+A_{\text{pr}}} \rangle_t - \langle \hat{J}_A \rangle_t \right) = \int_{-\infty}^t \sigma(t, t') E_{\text{pr}}(t') dt', \quad (4)$$

where L is the system size and $\sigma(t, t')$ represents the linear-response function for electric field. Since the response function should satisfy causality, i.e., $\sigma(t, t') = \theta(t - t')\sigma(t, t')$, we obtain $j_{\text{pr}}(\omega) = \int \sigma(\omega, t')E_{\text{pr}}(t')e^{i\omega t'} dt'$ by Fourier transformation. Assuming that the probe pulse $E_{\text{pr}}(t)$ persists only during $t_{\text{pr}} \pm \tau/2$ and τ is much smaller than the characteristic time scale of the system, we can approximate $j_{\text{pr}}(\omega) \simeq \sigma(\omega, t_{\text{pr}}) \int E_{\text{pr}}(t')e^{i\omega t'} dt'$ [42]. In this case, the optical conductivity of the frequency ω at probe time t_{pr} can be evaluated from

$$\sigma(\omega, t_{\text{pr}}) = \frac{j_{\text{pr}}(\omega)}{i(\omega + i\eta)A_{\text{pr}}(\omega)}, \quad (5)$$

where $A_{\text{pr}}(\omega) = E_{\text{pr}}(\omega)/i(\omega + i\eta)$ with a damping factor η . Even though this factor is introduced for the convergence of our numerical Fourier transformation, it is associated with the lifetime of the quasiparticles due to, for example, impurity scattering in actual materials. In this way, we can directly determine equilibrium and nonequilibrium optical conductivities in the thermodynamic limit by means of the iTEBD method. We adopt a weak, narrow probe pulse $A_{\text{pr}}(t) = A_{0,\text{pr}}e^{-(t-t_{\text{pr}})^2/2\sigma_{\text{pr}}^2}$ as the infinitesimal external field. When σ_{pr} is sufficiently small compared to the characteristic time scale of the system and $\omega A_{0,\text{pr}}\sqrt{2\pi}\sigma_{\text{pr}} \ll 1$ is satisfied, the optical conductivity obtained by this method reproduces the result calculated by Kubo formula [42]. Note that in previous studies [37, 38, 42–44], the same method was used, but only for finite-size systems, in order to simulate the nonequilibrium optical conductivity. In the following, we set $A_{0,\text{pr}} = 0.05$, $\sigma_{\text{pr}} = 0.05$, and $\eta = 0.1$ for the computations of optical conductivity. We denote $\Delta t_{\text{pr}} = t_{\text{pr}} - t_0$ and rewrite Eq. (5) as $\sigma(\omega, \Delta t_{\text{pr}})$.

Figure 1(a) shows the real parts of the optical conductivity of the SDW states for $U = 10$ and various V in the absence of the pump pulse [$A(t) = 0$], which is consistent with previous dynamical density-matrix renormalization group studies [45, 46]. A broad peak appears above a charge gap at $V = 0$, originating from the excitations between the continuum of upper and lower Hubbard bands. Turning on the intersite interaction V , the energy level of a doublon-holon bound state (exciton) emerges, and decreases as V increases. The energy level of the exciton becomes smaller than the bottom of the energy continuum for $V \geq 2$, leading to the emergence of a sharp peak below the charge gap [47]. We should note that in our numerical calculations, the amplitude of this excitonic peak is finite due to the finite η and diverges as $\eta \rightarrow 0$ [46]. The excitonic energy level becomes the lowest value at the SDW-CDW transition point $V \simeq U/2$.

The optical conductivities of the CDW state $V > U/2$ are shown in Fig. 1(b). Here, the peak position of $\text{Re } \sigma(\omega)$ increases as V increases. This peak position corresponds to the energy required to dissociate a doublon.

The peak positions of the optical conductivities can be readily estimated in the strong-coupling limit ($U, V \gg$

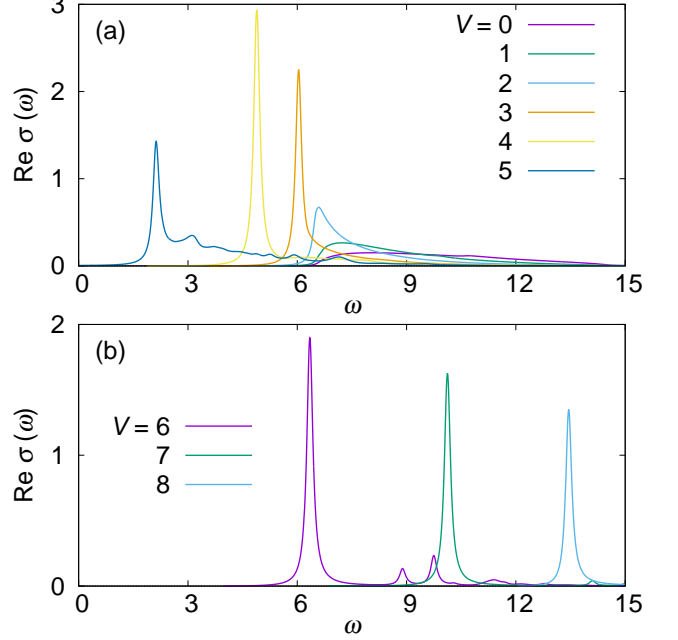


FIG. 1. The real part of the optical conductivity of the 1DEHM for $U = 10$ in the GS at (a) SDW phase ($V \leq U/2$) and (b) CDW phase ($V > U/2$). The damping factor is set to $\eta = 0.1$.

t_h). In this limit, the SDW state comprises singly-occupied sites. Thus, the energy of the first-excited state, characterized by the presence of an adjacent doublon and holon, is approximately $U - V$. On the other hand, doublons and holons align alternately in the CDW state. Therefore, the first-excited state, where two adjacent sites become singly-occupied, requires an excitation energy of approximately $3V - U$.

A. SDW phase

We first show the nonequilibrium optical conductivity of the 1DEHM with $U = 10$ and $V = 3$ in Fig. 2. The pump-pulse frequency is set to $\omega_0 = 6.04$, where $\text{Re } \sigma(\omega)$ reaches its maximum, see Fig. 1(a). By comparing the spectra obtained at $\Delta t_{\text{pr}} = 0$ with those in the absence of the pump pulse, we observe two characteristic features. One is the large negative spectra at the pump-light frequency $\omega = \omega_0$, which may originate from the population inversion of the electrons due to the pump-pulse irradiation. This nonthermal state leads to stimulated emission by the probe pulse, resulting in the negative optical conductivity [48]. The other is the emergence of a new peak at small ω , which implies the creation of an in-gap state. This in-gap state is associated with two types of excitons in the 1DEHM: even- and odd-parity excitons [37]. The energy level of the even-parity excitons is slightly

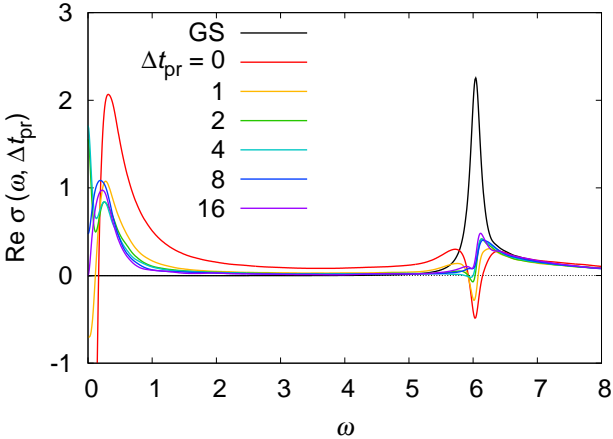


FIG. 2. The real part of nonequilibrium optical conductivity of the 1DEHM at $U = 10$ and $V = 3$ (SDW phase) for various probe times. The black solid line indicates the optical conductivity in the GS.

larger than that of the odd-parity excitons, and the optical transitions to the even-parity excitons from the GS are forbidden [49–51]. However, once a state enters the odd-parity excitonic state due to the pump pulse, the state can be further excited to an even-parity exciton level by the subsequent probe pulse. Therefore, transitions to the even-parity excitonic state, which are not allowed from the GS, are realized.

Once the pump pulse has passed, the system begins to relax via the recombination of doublons and holons. The negative spectra at $\omega = \omega_0$ gradually turn into positive asymmetric ones, which implies the emergence of Fano resonance. In this case, there is a quantum interference between the exciton level and the doublon-holon continuum [38]. On the other hand, the in-gap state remains over time. The reason why the peak position with regard to the in-gap state at $\Delta t_{\text{pr}} > 0$ becomes smaller than that at $\Delta t_{\text{pr}} = 0$ can be attributed to the Stark effect of the excitons [52, 53]. The electric field of the pump pulse at $\Delta t_{\text{pr}} = 0$ enhances the splitting between the even- and odd-parity exciton levels. The energy of the in-gap state eventually stabilizes at approximately $\omega = 0.2$.

To further scrutinize the aforementioned features, we also examine the SDW state with a larger interaction strength. Figure 3 shows the nonequilibrium optical conductivity at $U = 20$ and $V = 6$ with $\omega_0 = 13.55$. We find that, in addition to the peak originating from two exciton levels at small ω , labeled as α , there are two broad structures (β and γ) and a sharp peak at $\omega = 10.5$ (δ) below the optical gap. Moreover, a new peak arises at $\omega = 21.1$ (ε), which is located at a higher energy than the exciton level. Apart from the peak α , the origins of these peaks can be better understood from the numerical results of nonequilibrium single-particle excitation spectra, which we will discuss in the subsequent section.

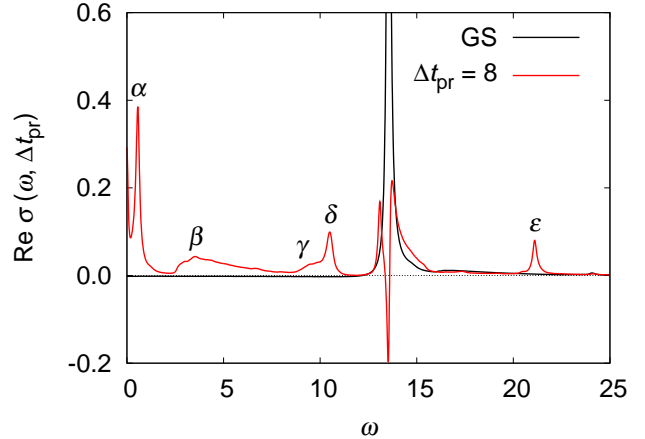


FIG. 3. The real part of the nonequilibrium optical conductivity of the 1DEHM at $U = 20$ and $V = 6$ (SDW phase). The black and red solid lines are for the GS and the nonequilibrium state at $\Delta t_{\text{pr}} = 8$, respectively. The labels above the spectrum denote the new peaks that arise in the nonequilibrium state.

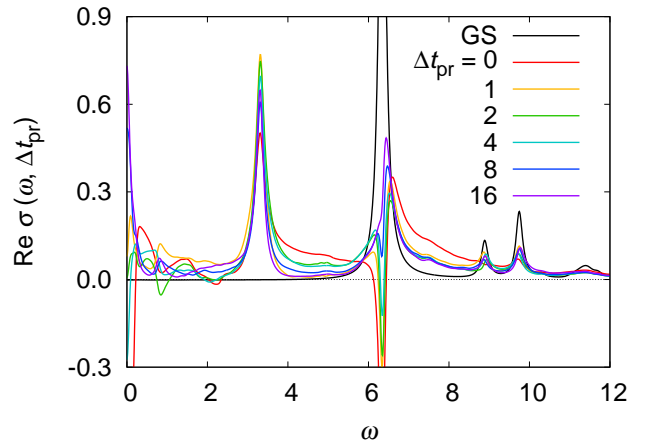


FIG. 4. The real part of the nonequilibrium optical conductivity of the 1DEHM at $U = 10$ and $V = 6$ (CDW phase) for various probe times. The black solid line indicates the optical conductivity in the GS.

B. CDW phase

Figure 4 illustrates the real part of the nonequilibrium optical conductivity upon application of the pump pulse with $\omega_0 = 6.34$ to the CDW state with $U = 10$ and $V = 6$. Similar to the SDW phase, the pump-pulse irradiation results in a prominent negative spectrum at $\omega = \omega_0$. Following the passage of the pump pulse, the spectral weight at this energy recovers to positive values, eventually forming an asymmetric spectrum.

A notable change is the emergence of a new state at $\omega = 3.3$ in the nonequilibrium state, which is consistent

with the previous study [37]. This in-gap state can be interpreted from the newly formed bands in the single-particle spectra, as we will be discussed later.

We also observe messy spectral structures for $\omega < 2$ that are newly generated and strongly time-dependent. The system relaxes to a steady state over time, and the Drude weight (spectrum at $\omega = 0$) becomes finite, suggesting photoinduced metallization.

IV. TIME- AND ANGLE-RESOLVED PHOTOEMISSION SPECTRA

We now discuss the time-dependent single-particle excitation spectra in the 1DEHM, taking into account TARPES experiments. The intensity of single-particle excitation spectra with momentum k and energy ω is given by [54, 55]

$$A^-(k, \omega, \Delta t_{\text{pr}}) = \frac{1}{L} \sum_{j, \ell, \sigma} e^{-ik(r_j - r_\ell)} \int_{-\infty}^{\infty} dt_1 \int_{-\infty}^{\infty} dt_2 e^{i\omega(t_1 - t_2)} \times s(t_1 - t_{\text{pr}}) s(t_2 - t_{\text{pr}}) \langle \hat{c}_{\ell, \sigma}^\dagger(t_2, -\infty) \hat{c}_{j, \sigma}(t_1, -\infty) \rangle_{-\infty}, \quad (6)$$

where $s(t - t_{\text{pr}})$ is an envelope function of the wave packet of the probe pulse at time t_{pr} and $\hat{c}_{j, \sigma}(t, t') = \hat{U}^\dagger(t, t') \hat{c}_{j, \sigma} \hat{U}(t, t')$ is the Heisenberg representation. The envelope function utilized in this study is a Gaussian function written as

$$s(t - t_{\text{pr}}) = \frac{1}{\sqrt{2\pi}\sigma_{\text{pr}}} \exp\left(-\frac{(t - t_{\text{pr}})^2}{2\sigma_{\text{pr}}^2}\right), \quad (7)$$

where σ_{pr} represents the width of the wave packet. To simulate single particle excitation spectra in nonequilibrium, we construct the window state from the iMPS obtained from the iTEBD method and employ the infinite-boundary conditions with a uniform update scheme [56]. For more detail, refer to Ref. [57]. We find that the size of the window state, $L_w = 64$, is sufficient for the present case. In addition, we define the integrated photoemission spectra as

$$A^-(\omega, \Delta t_{\text{pr}}) = \int_{-\pi}^{\pi} \frac{dk}{2\pi} A^-(k, \omega, \Delta t_{\text{pr}}), \quad (8)$$

which in the following will be denoted as the time-resolved density of states (TDOS). In this section, we set the probe-pulse width as $\sigma_{\text{pr}} = 3$.

A. SDW phase

Let us first recall the results of single-particle excitation spectra in the pure Hubbard model, i.e., $V = 0$ in

Eq. (1), as shown in upper panels of Fig. 5, which have also been discussed in Ref. [57].

In the absence of the pump pulse [$A(t) = 0$], the Bethe ansatz [58, 59] provides the exact energy dispersion, which explains the results for $U = 10$ in Fig. 5(a). There are one spinon and two holon bands due to spin-charge separation. The two holon bands are degenerate at $k = 0$ and $\pm\pi$, and their width is $4t_h$. The spinon and holon bands split at $k = 0$, while the upper holon band merges with the spinon band at $k = \pm\pi$. The spinon-holon excitation continuum below the lower holon band is visible for $|k| \geq \pm\pi/2$. The spectra obtained here correspond to the lower Hubbard band. A detailed comparison of the exact results and the calculated spectra can be found in Refs. [60–62].

We now turn to the case for the nonequilibrium state. It should be noted that this photoexcited state is associated with the emergence of the so-called η -pairing state [63–66], which is the exact eigenstate of the Hubbard model [59, 67]. Figures 5(b) and 5(c) respectively show $A^-(k, \omega, \Delta t_{\text{pr}})$ at $\Delta t_{\text{pr}} = 0$ and $\Delta t_{\text{pr}} = 8$. The pump pulse induces a photoexcited state, leading to the emergence of a new dispersion with its minimum at $k = 0$, ranging from $k = -\pi$ to π above the Fermi level, and a reduction in the spectral intensity of the lower Hubbard band. This newly emerged dispersion is not seen in the inverse photoemission spectra [61]. The shift of the spectral weight after pulse irradiation can also be confirmed in the results of the TDOS, see Fig. 5(d).

Next, we introduce intersite interactions. Figure 5(e) shows the single-particle excitation spectra in the GS of the 1DEHM for $U = 10$ and $V = 3$. By introducing V , the charge gap becomes slightly smaller; however, the dispersion relation is almost the same as for the case of $V = 0$. We also find weak but new spectral weights around $k = \pm\pi/2$ and $\omega = -10.3$ appearing below the lower Hubbard band. While it is slightly difficult to see them in the intensity plot of Fig. 5(e), they can be recognized in the DOS illustrated in Fig. 5(h) as a black solid line.

Figures 5(f) and 5(g) show $A^-(k, \omega, \Delta t_{\text{pr}})$ after the pump pulse irradiation. In this case, the pump pulse creates numerous doublons and holons, leading to the formation of excitons due to the nonlocal interactions. We find a new dispersion above the Fermi level, as in the case of $V = 0$. However, unlike the case of $V = 0$, this dispersion has the maximum at $k = \pm\pi/2$. The difference between the maximum energy of the newly emerged band and that of the lower Hubbard band is almost equal to the excitonic energy, estimated from the peak position of the optical conductivity [$\omega \simeq 6.04$, see Fig. 1(a)]. Therefore, we can interpret that the new dispersion originates from the excitons created by the pump pulse. This new band has the same dispersion as the lower Hubbard band and its visibility increases with the intensity of the pump pulse (not shown here).

To better clarify the state under the creation of excitons by the pump pulse in the SDW phase, we also

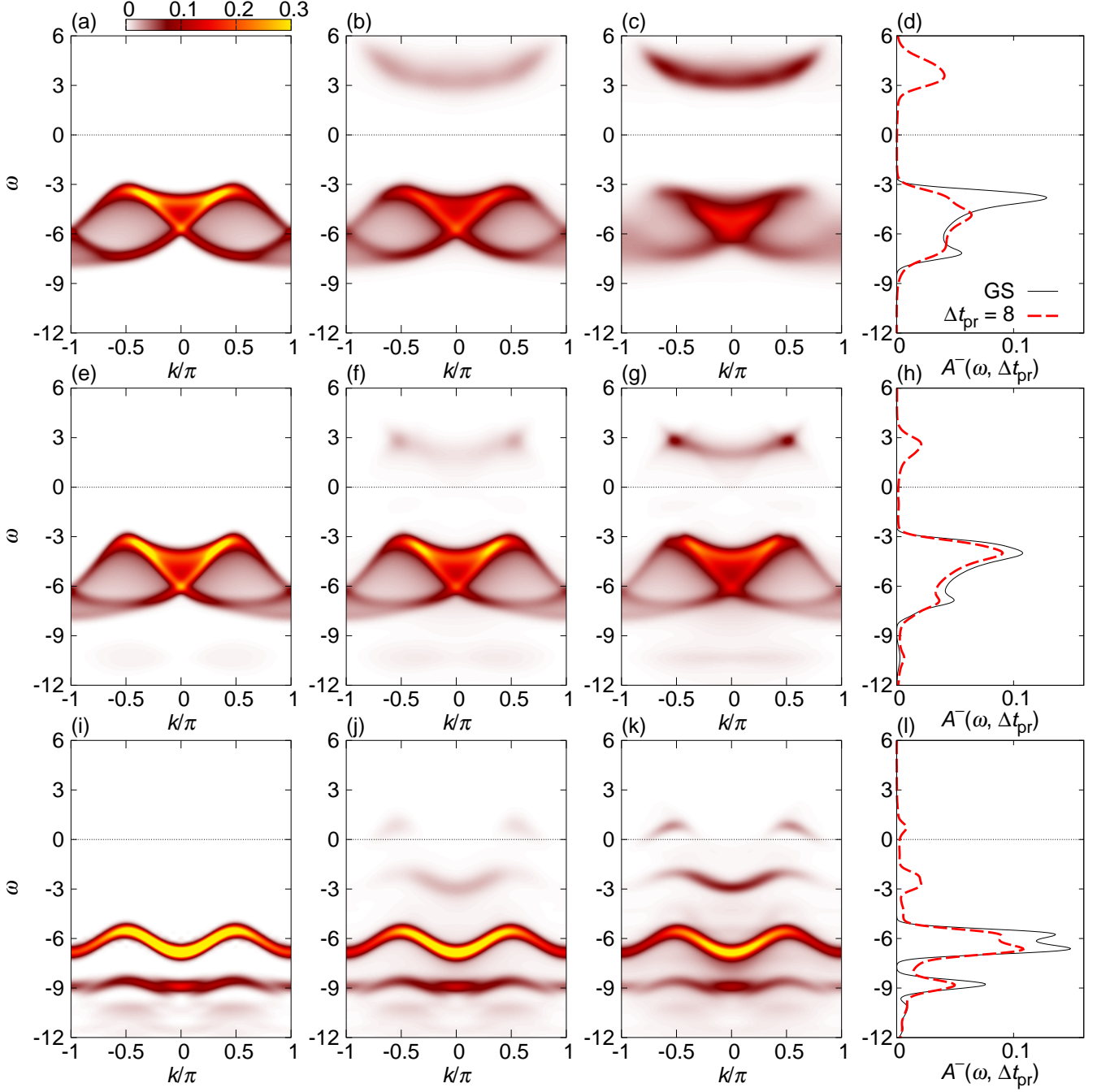


FIG. 5. [(a)-(c), (e)-(g), and (j)-(k)] Calculated single-particle excitation spectra of the 1DEHM at [(a), (e), and (i)] $\Delta t_{\text{pr}} = -\infty$ (GS), [(b), (f), and (j)] $\Delta t_{\text{pr}} = 0$, and [(c), (g), and (k)] $\Delta t_{\text{pr}} = 8$. [(d), (h), and (l)] TDOSs at $\Delta t_{\text{pr}} = -\infty$ (black solid line) and $\Delta t_{\text{pr}} = 8$ (red dashed line). The on-site interaction is set to $U = 10$, and the intersite interaction is set to [(a)-(d)] $V = 0$, [(e)-(h)] $V = 3$, and [(i)-(l)] $V = 6$.

present the results with larger interaction parameters. Figure 6(a) shows the single-particle excitation spectra in the GS at $U = 20$ and $V = 6$. Reflecting the large interaction parameters, the lower Hubbard band appears at a lower energy level. Figure 6(b) shows $A^-(k, \omega, \Delta t_{\text{pr}})$ after the pump-pulse irradiation, which resembles the dis-

persions obtained by the interaction quench [68]. A new dispersion with the same shape as the lower Hubbard band appears above the Fermi level. The energy difference between the new bands and the lower Hubbard bands is the same as the excitonic energy estimated from the peak position of $\sigma(\omega)$ ($\omega \simeq 13.55$, see Fig. 3).

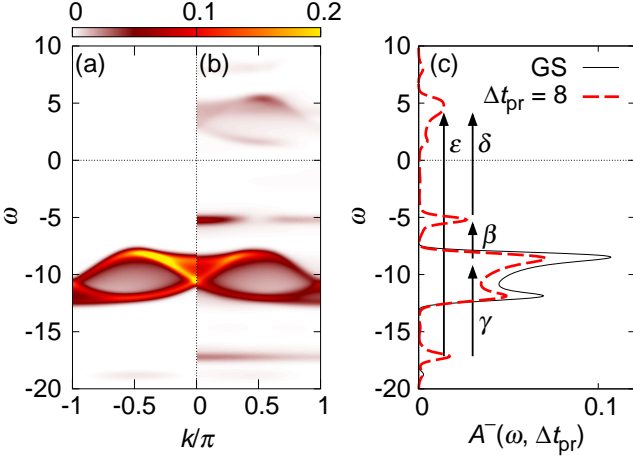


FIG. 6. Calculated single-particle excitation spectra of the 1DEHM for $U = 20$ and $V = 6$ at (a) $\Delta t_{\text{pr}} = -\infty$ (GS) and (b) $\Delta t_{\text{pr}} = 8$. (c) The TDOS at $\Delta t_{\text{pr}} = -\infty$ (black solid line) and $\Delta t_{\text{pr}} = 8$ (red dashed line). The arrows in the TDOS correspond to the optical excitations observed in the nonequilibrium optical conductivity in Fig. 3.

Furthermore, dispersionless flat bands, which may be associated with charge-order fluctuations, also appear both above and below the lower Hubbard band [33, 68]. Recall that, in the nonequilibrium optical conductivity after the pump-pulse irradiation, four peaks β , γ , δ , and ε emerge in addition to the peak α originating from the excitation between different parity excitons (see Fig. 3). By comparing the peak positions in the optical conductivity with the energy-level differences of the peaks in the DOS, we can identify that the broad peak β is ascribed to the excitation from the lower Hubbard band to the flat band, the hump structure γ originates from the excitation from the flat band to the lower Hubbard band, and the two peaks γ and ε arise from the excitation from the flat bands to the newly emerging bands above the Fermi level. The corresponding optical excitations are depicted by black arrows in Fig. 6(c).

B. CDW phase

Finally, we examine the time-dependent single-particle excitation spectra in the CDW phase, as shown in the lower panels of Fig. 5 for $U = 10$ and $V = 6$. Under the formation of charge ordering in the GS, the two holon bands, which are degenerate at $k = 0$ and $\pm\pi$ in the SDW phase, split into a band with a cosine-type dispersion centered at $\omega = 6$ and a relatively flat band centered at $\omega = 9$. Figures 5(j) and 5(k) show $A^-(k, \omega, \Delta t_{\text{pr}})$ under the influence of the pump pulse. Two new dispersions emerge around the Fermi level. These results have been previously reported by exact diagonalization for small clusters [69]. Thanks to the higher-resolution spectra obtained directly in the thermodynamic limit, the ex-

citation from the band around $\omega = -6$ to the one around $\omega = -2.7$ can be significantly distinguished, which is related to the in-gap state observed in the nonequilibrium optical conductivity shown in Fig. 4.

V. CONCLUSIONS AND OUTLOOK

We explored the pump-probe spectroscopy of the 1DEHM at half filling in an infinite system. In the strong-coupling regime, the GS of this model resides in the SDW phase when $U \lesssim 2V$ and in the CDW phase when $U \gtrsim 2V$. In the SDW phase, doublons and holons, which is generated by the intense pump pulse, form bound states known as excitons through nonlocal interactions. In the CDW phase, the charge order dissolves due to photoexcitation. The dynamical response in the nonequilibrium state was revealed using the iTEBD method.

We detected an in-gap state at small ω in the nonequilibrium optical conductivity for the model with $U = 10$ and $V = 3$, which resides in the SDW phase. This state can be interpreted as the transition between the odd-parity exciton and the even-parity exciton. Furthermore, we investigated a stronger interaction model with $U = 20$ and $V = 6$. In addition to this in-gap state originating from the different parity excitons, we discovered that additional peaks appear below and above the excitonic energy. The origin of these additional peaks can be understood by examining the single-particle excitation spectra. Specifically, the new dispersions appearing above and below the lower Hubbard band after the pump pulse irradiation are associated with these new peaks in the optical conductivity. We also observed that the lower Hubbard bands are replicated in a higher energy region, where the energy difference is equal to the excitonic energy.

Moreover, we examined the nonequilibrium optical conductivity for the model with $U = 10$ and $V = 6$, which resides in the CDW phase. In this case, we also found an in-gap state after the pump pulse irradiation. Additionally, we discovered that the Drude weight becomes finite, suggesting the metallization of the system. The origin of this in-gap state can be understood from the single-particle excitation spectra.

Lastly, we address the correspondence between our theoretical findings and experimental observations. The 1D Mott insulator ET-F₂TCNQ is well described by the 1DEHM with interaction parameters $U = 10$ and $V = 3$ [51]. In fact, the emergence of the in-gap state in the optical conductivity after the pump pulse irradiation has been observed. Thus, the single-particle excitation spectra obtained in this study are also expected to be observed in this material by TARPES. Another approach to realizing our results is by employing a cold atomic system [70]. With an artificial gauge field mimicking the pump pulse, the observation of single-particle excitation spectra may be feasible. It is worth emphasizing that our calculations, performed on an infinite system, allow

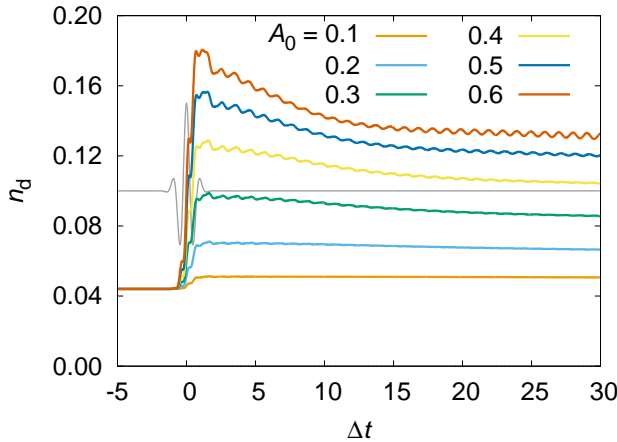


FIG. 7. The double occupancies of the 1DEHM at $U = 10$ and $V = 3$ for various A_0 as functions of time. The gray solid line indicates the time dependence of the pump pulse $A(t)$. We denote $\Delta t = t - t_0$ in the horizontal axis, where t_0 is the central time of the pump pulse.

for a direct comparison of the spectra observed in future experiments with our results.

In this study, our focus was on nonequilibrium optical conductivity and single-particle excitation spectra. Recently, time-resolved resonant inelastic x-ray scattering (RIXS) spectra have become observable through pump-probe spectroscopy [71–73]. RIXS allows us to examine the dynamical correlations of charge and spin, including their momentum dependence, thereby enabling us to obtain more detailed information on strongly correlated materials. We anticipate further developments in theoretical studies of pump-probe spectroscopy using iMPS in the future.

ACKNOWLEDGMENTS

K.S. was supported by JSPS KAKENHI Grant Numbers JP20H01849, JP21K03439, and JP23K03286. The iTEBD calculations were performed using the ITensor library [74].

Appendix A: Double occupancy

Figure 7 shows the double occupancies

$$n_d(t) = \frac{1}{L} \sum_j \langle \hat{n}_{j,\uparrow} \hat{n}_{j,\downarrow} \rangle_t \quad (A1)$$

of the extended Hubbard model at $U = 10$ and $V = 3$ as functions of time, for various pump-pulse intensities. Upon the pump-pulse irradiation, doublons and holons are generated, leading to an increase in double occupancy. Following the passing of the pump light, the system begins to gradually relax through the recombination of doublons and holons.

The larger the value of A_0 , the more significant the increase in the double occupancy. When a state is intensely excited by a pump pulse, the entanglement of the quantum state evolves throughout the system, suggesting that the system can no longer be described by the iMPS. Specifically, the truncation error reaches up to 4×10^{-5} in the calculation with $A_0 = 0.6$. For $A_0 = 0.3$, we confirmed that the truncation error is suppressed to below 4×10^{-6} .

Appendix B: Linear response theory of optical conductivity

In an ideal scenario, the optical conductivity should be calculated using Kubo formula, which is based on the linear response theory and requires the calculation of current-current correlation functions [38, 42, 75, 76]. This process necessitates the creation of a window state with infinite-boundary conditions [56, 57] and the application of the local current operator at the center of the window state. Given the requirement for long-time simulation to derive optical conductivities, the influence of the local current operator applied at the center site extends to the boundary before the calculation is finished. We determined that, for a damping factor of $\eta = 0.1$, a window state of size $L_w > 128$ should be prepared. As this incurs substantial computational cost, we have chosen to employ the method delineated in the main text.

Appendix C: TARPES and Green's function

By definition, Eq. (6) equals to

$$\begin{aligned} & A^-(k, \omega, \Delta t_{\text{pr}}) \\ &= \frac{1}{L} \sum_{j,\ell,\sigma} e^{-ik(r_j - r_\ell)} \int_{-\infty}^{\infty} dt_1 \int_{-\infty}^{\infty} dt_2 e^{i\omega(t_1 - t_2)} \\ & \quad \times s(t_1 - t_{\text{pr}}) s(t_2 - t_{\text{pr}}) \langle \psi(t_2) | \hat{c}_{\ell,\sigma}^\dagger \hat{U}(t_2, t_1) \hat{c}_{j,\sigma} | \psi(t_1) \rangle. \end{aligned} \quad (C1)$$

Upon partitioning the integration range of t_2 into two regimes, $t_2 > t_1$ and $t_2 < t_1$, we derive

$$\begin{aligned}
A^-(k, \omega, \Delta t_{\text{pr}}) = & \frac{1}{L} \sum_{j, \ell, \sigma} e^{-ik(r_j - r_\ell)} \int_{-\infty}^{\infty} dt_1 \int_{-\infty}^{t_1} dt_2 e^{i\omega(t_1 - t_2)} s(t_1 - t_{\text{pr}}) s(t_2 - t_{\text{pr}}) \langle \psi(t_2) | \hat{c}_{\ell, \sigma}^\dagger \hat{U}(t_2, t_1) \hat{c}_{j, \sigma} | \psi(t_1) \rangle \\
& + \frac{1}{L} \sum_{j, \ell, \sigma} e^{-ik(r_j - r_\ell)} \int_{-\infty}^{\infty} dt_1 \int_{t_1}^{\infty} dt_2 e^{i\omega(t_1 - t_2)} s(t_1 - t_{\text{pr}}) s(t_2 - t_{\text{pr}}) \langle \psi(t_1) | \hat{c}_{j, \sigma}^\dagger \hat{U}(t_1, t_2) \hat{c}_{\ell, \sigma} | \psi(t_2) \rangle^*,
\end{aligned} \tag{C2}$$

and by replacing $\int_{-\infty}^{\infty} dt_1 \int_{-\infty}^{t_1} dt_2 = \int_{-\infty}^{\infty} dt_2 \int_{t_2}^{\infty} dt_1$ in the first term, Eq. (C2) becomes

$$\begin{aligned}
A^-(k, \omega, \Delta t_{\text{pr}}) = & \frac{1}{L} \sum_{j, \ell, \sigma} e^{-ik(r_j - r_\ell)} \int_{-\infty}^{\infty} dt_2 \int_{t_2}^{\infty} dt_1 e^{i\omega(t_1 - t_2)} s(t_1 - t_{\text{pr}}) s(t_2 - t_{\text{pr}}) \langle \psi(t_2) | \hat{c}_{\ell, \sigma}^\dagger \hat{U}(t_2, t_1) \hat{c}_{j, \sigma} | \psi(t_1) \rangle \\
& + \frac{1}{L} \sum_{j, \ell, \sigma} e^{-ik(r_j - r_\ell)} \int_{-\infty}^{\infty} dt_1 \int_{t_1}^{\infty} dt_2 e^{i\omega(t_1 - t_2)} s(t_1 - t_{\text{pr}}) s(t_2 - t_{\text{pr}}) \langle \psi(t_1) | \hat{c}_{j, \sigma}^\dagger \hat{U}(t_1, t_2) \hat{c}_{\ell, \sigma} | \psi(t_2) \rangle^* \\
= & 2 \text{Im} \left[\frac{1}{L} \sum_{j, \ell, \sigma} e^{-ik(r_j - r_\ell)} \int_{-\infty}^{\infty} dt_2 \int_{t_2}^{\infty} dt_1 e^{i\omega(t_1 - t_2)} s(t_1 - t_{\text{pr}}) s(t_2 - t_{\text{pr}}) G_{j\ell}^<(t_1, t_2) \right],
\end{aligned} \tag{C3}$$

where $G_{j\ell}^<(t_1, t_2) = i \langle \psi(t_2) | \hat{c}_{\ell, \sigma}^\dagger \hat{U}(t_2, t_1) \hat{c}_{j, \sigma} | \psi(t_1) \rangle$ is the lesser Green's function. Initially, we calculate a sequence of iMPS for each time by the iTEBD method. Subsequently, we generate window states corresponding to

$\hat{U}(t_1, t_2) \hat{c}_{\ell, \sigma} | \psi(t_2) \rangle$ and $\hat{c}_{j, \sigma} | \psi(t_1) \rangle$. By evaluating the inner product of these states, we deduce the integrand of Eq. (C3).

[1] A. de la Torre, D. M. Kennes, M. Claassen, S. Gerber, J. W. McIver, and M. A. Sentef, *Rev. Mod. Phys.* **93**, 041002 (2021).

[2] T. Dong, S.-J. Zhang, and N.-L. Wang, *Adv. Mater.* **2022**, 2110068 (2022).

[3] S. Kaiser, *Phys. Scr.* **92**, 103001 (2017).

[4] A. Cavalleri, *Contemp. Phys.* **59**, 31 (2018).

[5] D. Fausti, R. I. Tobey, N. Dean, S. Kaiser, A. Dienst, M. C. Hoffmann, S. Pyon, T. Takayama, H. Takagi, and A. Cavalleri, *Science* **331**, 189 (2011).

[6] T. Suzuki, T. Someya, T. Hashimoto, S. Michimae, M. Watanabe, M. Fujisawa, T. Kanai, N. Ishii, J. Itatani, S. Kasahara, Y. Matsuda, T. Shibauchi, K. Okazaki, and S. Shin, *Commun. Phys.* **2**, 115 (2019).

[7] K. Isoyama, N. Yoshikawa, K. Katsumi, J. Wong, N. Shikama, Y. Sakishita, F. Nabeshima, A. Maeda, and R. Shimano, *Commun. Phys.* **4**, 160 (2021).

[8] M. Buzzi, D. Nicoletti, M. Fechner, N. Tancogne-Dejean, M. A. Sentef, A. Georges, T. Biesner, E. Uykur, M. Dresel, A. Henderson, T. Siegrist, J. A. Schlueter, K. Miyagawa, K. Kanoda, M.-S. Nam, A. Ardavan, J. Coulthard, J. Tindall, F. Schlawin, D. Jaksch, and A. Cavalleri, *Phys. Rev. X* **10**, 031028 (2020).

[9] P. Werner, H. U. R. Strand, S. Hoshino, Y. Murakami, and M. Eckstein, *Phys. Rev. B* **97**, 165119 (2018).

[10] Y. Wang, C.-C. Chen, B. Moritz, and T. P. Devereaux, *Phys. Rev. Lett.* **120**, 246402 (2018).

[11] N. Bittner, T. Tohyama, S. Kaiser, and D. Manske, *J. Phys. Soc. Jpn.* **88**, 044704 (2019).

[12] F. Schlawin, A. Cavalleri, and D. Jaksch, *Phys. Rev. Lett.* **122**, 133602 (2019).

[13] P. Werner, J. Li, D. Golež, and M. Eckstein, *Phys. Rev. B* **100**, 155130 (2019).

[14] A. Kirilyuk, A. V. Kimel, and T. Rasing, *Rev. Mod. Phys.* **82**, 2731 (2010).

[15] S. Ishihara, *J. Phys. Soc. Jpn.* **88**, 072001 (2019).

[16] R. Mikhaylovskiy, E. Hendry, A. Secchi, J. Mentink, M. Eckstein, A. Wu, R. Pisarev, V. Kruglyak, M. Katsnelson, T. Rasing, and A. Kimel, *Nat. Commun.* **6**, 8190 (2015).

[17] S. Baierl, M. Hohenleutner, T. Kampfrath, A. K. Zvezdin, A. V. Kimel, R. Huber, and R. V. Mikhaylovskiy, *Nat. Photon.* **10**, 715 (2016).

[18] D. Afanasiev, A. Gatilova, D. J. Groenendijk, B. A. Ivanov, M. Gibert, S. Gariglio, J. Mentink, J. Li, N. Dasari, M. Eckstein, T. Rasing, A. D. Caviglia, and A. V. Kimel, *Phys. Rev. X* **9**, 021020 (2019).

[19] S. Schlauderer, C. Lange, S. Baierl, T. Ebnet, C. P. Schmid, D. C. Valovcin, A. K. Zvezdin, A. V. Kimel, R. V. Mikhaylovskiy, and R. Huber, *Nature* **569**, 383 (2019).

[20] J. H. Mentink, K. Balzer, and M. Eckstein, *Nat. Commun.* **6**, 6708 (2015).

[21] J. Li, H. U. R. Strand, P. Werner, and M. Eckstein, *Nat. Commun.* **9**, 4581 (2018).

[22] H. Okamoto, H. Matsuzaki, T. Wakabayashi, Y. Takahashi, and T. Hasegawa, *Phys. Rev. Lett.* **98**, 037401 (2007).

[23] H. Uemura, H. Matsuzaki, Y. Takahashi, T. Hasegawa, and H. Okamoto, *J. Phys. Soc. Jpn.* **77**, 113714 (2008).

[24] S. Wall, D. Brida, S. R. Clark, H. P. Ehrke, D. Jaksch, A. Ardavan, S. Bonora, H. Uemura, Y. Takahashi, T. Hasegawa, H. Okamoto, G. Cerullo, and A. Cavalieri, *Nat. Phys.* **7**, 114 (2011).

[25] T. Miyamoto, T. Kakizaki, T. Terashige, D. Hata, H. Yamakawa, T. Morimoto, N. Takamura, H. Yada, Y. Takahashi, T. Hasegawa, H. Matsuzaki, T. Tohyama, and H. Okamoto, *Commun. Phys.* **2**, 131 (2019).

[26] N. Takamura, T. Miyamoto, S. Liang, K. Asada, T. Terashige, Y. Takahashi, T. Hasegawa, and H. Okamoto, *Phys. Rev. B* **107**, 085147 (2023).

[27] S. Iwai, M. Ono, A. Maeda, H. Matsuzaki, H. Kishida, H. Okamoto, and Y. Tokura, *Phys. Rev. Lett.* **91**, 057401 (2003).

[28] H. Matsuzaki, M. Yamashita, and H. Okamoto, *J. Phys. Soc. Jpn.* **75**, 123701 (2006).

[29] H. Matsuzaki, M. Iwata, T. Miyamoto, T. Terashige, K. Iwano, S. Takaishi, M. Takamura, S. Kumagai, M. Yamashita, R. Takahashi, Y. Wakabayashi, and H. Okamoto, *Phys. Rev. Lett.* **113**, 096403 (2014).

[30] H. Gomi, A. Takahashi, T. Ueda, H. Itoh, and M. Aihara, *Phys. Rev. B* **71**, 045129 (2005).

[31] K. A. Al-Hassanieh, F. A. Reboredo, A. E. Feiguin, I. González, and E. Dagotto, *Phys. Rev. Lett.* **100**, 166403 (2008).

[32] A. Takahashi, H. Itoh, and M. Aihara, *Phys. Rev. B* **77**, 205105 (2008).

[33] H. Lu, S. Sota, H. Matsueda, J. Bonča, and T. Tohyama, *Phys. Rev. Lett.* **109**, 197401 (2012).

[34] C. Shao, H. Lu, H.-G. Luo, and R. Mondaini, *Phys. Rev. B* **100**, 041114(R) (2019).

[35] Y. Murakami, S. Takayoshi, T. Kaneko, Z. Sun, D. Golež, A. J. Millis, and P. Werner, *Commun. Phys.* **5**, 23 (2022).

[36] Y. Murakami, S. Takayoshi, T. Kaneko, A. M. Läuchli, and P. Werner, *Phys. Rev. Lett.* **130**, 106501 (2023).

[37] H. Lu, C. Shao, J. Bonča, D. Manske, and T. Tohyama, *Phys. Rev. B* **91**, 245117 (2015).

[38] J. Rincón and A. E. Feiguin, *Phys. Rev. B* **104**, 085122 (2021).

[39] S. Ejima and S. Nishimoto, *Phys. Rev. Lett.* **99**, 216403 (2007).

[40] G. Vidal, *Phys. Rev. Lett.* **98**, 070201 (2007).

[41] R. Orús and G. Vidal, *Phys. Rev. B* **78**, 155117 (2008).

[42] C. Shao, T. Tohyama, H.-G. Luo, and H. Lu, *Phys. Rev. B* **93**, 195144 (2016).

[43] K. Shinjo and T. Tohyama, *Phys. Rev. B* **98**, 165103 (2018).

[44] K. Shinjo, S. Sota, and T. Tohyama, *Phys. Rev. Res.* **4**, L032019 (2022).

[45] E. Jeckelmann, *Phys. Rev. B* **66**, 045114 (2002).

[46] E. Jeckelmann, *Phys. Rev. B* **67**, 075106 (2003).

[47] F. B. Gallagher and S. Mazumdar, *Phys. Rev. B* **56**, 15025 (1997).

[48] V. Ryzhii, M. Ryzhii, and T. Otsuji, *J. Appl. Phys.* **101**, 083114 (2007).

[49] Y. Mizuno, K. Tsutsui, T. Tohyama, and S. Maekawa, *Phys. Rev. B* **62**, R4769 (2000).

[50] H. Matsueda, T. Tohyama, and S. Maekawa, *Phys. Rev. B* **70**, 033102 (2004).

[51] T. Yamaguchi, K. Iwano, T. Miyamoto, N. Takamura, N. Kida, Y. Takahashi, T. Hasegawa, and H. Okamoto, *Phys. Rev. B* **103**, 045124 (2021).

[52] M. Udon, K. Sugimoto, T. Kaneko, and Y. Ohta, *Phys. Rev. B* **105**, L241108 (2022).

[53] M. Udon, T. Kaneko, and K. Sugimoto, “Wannier-stark ladders and stark shifts of excitons in mott insulators,” (2023), arXiv:2301.06075 [cond-mat.str-el].

[54] J. K. Freericks, H. R. Krishnamurthy, and T. Pruschke, *Phys. Rev. Lett.* **102**, 136401 (2009).

[55] J. K. Freericks, H. R. Krishnamurthy, M. A. Sentef, and T. P. Devereaux, *Phys. Scr.* **2015**, 014012 (2015).

[56] V. Zauner, M. Ganahl, H. G. Evertz, and T. Nishino, *J. Phys. Condens. Matter* **27**, 425602 (2015).

[57] S. Ejima, F. Lange, and H. Fehske, *Phys. Rev. Res.* **4**, L012012 (2022).

[58] E. H. Lieb and F. Y. Wu, *Phys. Rev. Lett.* **20**, 1445 (1968).

[59] F. H. L. Essler, H. Frahm, F. Göhmann, A. Klümper, and V. E. Korepin, *The One-Dimensional Hubbard Model* (Cambridge University Press, 2005).

[60] H. Benthien and E. Jeckelmann, *Phys. Rev. B* **75**, 205128 (2007).

[61] S. Ejima, F. Lange, and H. Fehske, *SciPost Phys.* **10**, 077 (2021).

[62] Y. Murakami, S. Takayoshi, A. Koga, and P. Werner, *Phys. Rev. B* **103**, 035110 (2021).

[63] T. Kaneko, T. Shirakawa, S. Sorella, and S. Yunoki, *Phys. Rev. Lett.* **122**, 077002 (2019).

[64] T. Kaneko, S. Yunoki, and A. J. Millis, *Phys. Rev. Res.* **2**, 032027(R) (2020).

[65] S. Ejima, T. Kaneko, F. Lange, S. Yunoki, and H. Fehske, *Phys. Rev. Res.* **2**, 032008(R) (2020).

[66] S. Ejima, T. Kaneko, F. Lange, S. Yunoki, and H. Fehske, *JPS Conf. Proc.* **30**, 011184 (2020).

[67] C. N. Yang, *Phys. Rev. Lett.* **63**, 2144 (1989).

[68] K. Zawadzki and A. E. Feiguin, *Phys. Rev. B* **100**, 195124 (2019).

[69] C. Shao, T. Tohyama, H.-G. Luo, and H. Lu, *Phys. Rev. B* **101**, 045128 (2020).

[70] A. Bohrdt, D. Greif, E. Demler, M. Knap, and F. Grusdt, *Phys. Rev. B* **97**, 125117 (2018).

[71] Y. Cao, D. G. Mazzone, D. Meyers, J. P. Hill, X. Liu, S. Wall, and M. P. M. Dean, *Philos. Trans. Royal Soc. A* **377**, 20170480 (2019).

[72] M. Mitrano and Y. Wang, *Commun. Phys.* **3**, 184 (2020).

[73] F. Gel'mukhanov, M. Odilius, S. P. Polyutov, A. Föhlisch, and V. Kimberg, *Rev. Mod. Phys.* **93**, 035001 (2021).

[74] M. Fishman, S. R. White, and E. M. Stoudenmire, *SciPost Phys. Codebases* **4** (2022).

[75] Z. Lenarčič, D. Golež, J. Bonča, and P. Prelovšek, *Phys. Rev. B* **89**, 125123 (2014).

[76] J. Ohara, Y. Kanamori, and S. Ishihara, *Phys. Rev. B* **88**, 085107 (2013).